


Power harvesting in a helicopter rotor using a piezo stack in the lag damper

Pieter H de Jong, Andre de Boer, Richard Loendersloot and Peter J M van der Hoogt

Journal of Intelligent Material Systems and Structures
0(0) 1–13
© The Author(s) 2012
Reprints and permissions:
sagepub.co.uk/journalsPermissions.nav
DOI: 10.1177/1045389X12460336
jim.sagepub.com


Abstract

A piezoelectrically augmented helicopter lag damper has been simulated for the purpose of harvesting electrical energy within the rotor of the aircraft. This energy can then be consumed locally for sensing, processing, and transmission of data to the cockpit. An 8.15-m radius rotor is considered, and in-plane rigid lagging motion forms the prime excitation of the damper. The piezoelectric stack is installed within the rod of the damper in such a manner that the stack is submitted to all damper loads. MATLAB and Simulink are used to simulate a simplified blade model. A number of electrical harvesting circuits are investigated, and the piezo stack is optimized for each circuit. Also the effect of nonlinear capacitance of the piezo material is investigated revealing a profound effect. The important design parameters are identified and optimized resulting in a power output of 5.1 W for a steady 130-knot forward flight profile.

Keywords

Energy harvesting, piezoelectric, structural health monitoring, autonomic structures, rotorcraft

Introduction

Currently, helicopter rotor blades are replaced after a conservative lifetime calculation. This calculation assumes an absolute worst case usage scenario as failure of a rotor is unacceptable. This results in blades being discarded while they are still capable of numerous flight hours. To more accurately determine the life span of the blades, extensive health monitoring systems are required within the blade.

Although electrical devices do exist in production helicopters, they generally consist only of deicing systems powered from the body of the aircraft via slip rings. Slip rings are maintenance intensive and sensitive to damage. Within the European Clean Sky–Green Rotorcraft project, structural health monitoring in the blades and methods of powering these systems are investigated. Power harvesting in the rotor is considered as a method to power the health monitoring systems, negating the need for additional chassis–rotor electrical interfaces.

The concept presented here is a piezo stack in line with the blade lag damper, allowing it to undergo the same loads. The lag damper is a component designed to suppress oscillations of the blade within the plane of rotation, preventing phenomena such as air and ground resonance. This energy dissipation is required for aerodynamic stability of the aircraft. Converting this energy into electricity provides an efficiency increase

as opposed to increasing engine load. The stack is alternately compressed and relaxed by the force resulting from the damper as the blade performs a lag motion due to varying drag. This generates a charge displacement in the stack. The damper is well suited for this application as it develops forces in the order of kilonewtons. Another characteristic is that this force is well defined due to a relief valve opening in the damper, implying a maximum of 9 kN. This maximum is easily achieved during forward flight as will be shown in the “Modeling” section.

This article reports on the simulation and numerical results concerning power harvesting using a piezo stack in series with the lag damper. A brief literature review of relevant material is presented first, “Modeling” and “Piezoelectric model” sections describe the dynamic model considered using a two-degree-of-freedom (2-DOF) system. In “Circuits and simulation results” section, the electrical circuits are discussed and simulated, and the results are presented for each circuit. The simulations are expanded to include nonlinear capacitance

Structural Dynamics and Acoustics group, University of Twente, Enschede, The Netherlands

Corresponding author:

Pieter H de Jong, University of Twente, Postbus 217, Enschede, 7500AE, The Netherlands.
Email: p.h.dejong@utwente.nl

models and temperature effects in section “Nonlinear capacitance model and temperature effects” and finally some conclusions are presented in section “Conclusion.”

Literature review

The bulk of research in power harvesting is toward the design (Harris et al., 2010; Jeon et al., 2005) and improvement (Dietl and Garcia, 2010; Zheng et al., 2009) of cantilever-type harvesters. Its properties of actuation using minimal force, compact construction, and easily tunable natural frequency make it an ideal device for most power harvesting applications. Despite the higher piezoelectric performance of the 33 mode, the stacks are rarely used due to their mechanical properties (Roundy, 2005). In particular, the high stiffness associated with a stack negates the piezoelectric advantage. Some applications have been investigated but typically an amplification mechanism is needed to match the available force with the stack dimensions (Feenstra et al., 2008), increasing weight and volume of the entire device. The large force generated by the lag damper requires no such amplification and allows for a stack to be placed directly in series with the damper, making this concept unique. Here, the 33-mode operation of the stack is used to its full extent.

An important aspect of a power harvesting system is the choice of the electronics connected to the piezoelectric element. A passive circuit such as direct current impedance matching (DCIM) is used for microscale applications. The small output is not sufficient to sustain the losses associated with active circuits (Jeon et al., 2005; Shu and Lien, 2006a). However, when the output reaches the order of milliwatts, active systems are the best choice, which greatly increase the specific output of the material. Examples are the synchronous electric charge extraction (SECE) circuit (Lefevre et al., 2005) and the Synchronized Switch Harvesting on Inductor (SSHI) circuit (Guyomar et al., 2005; Lallart and Guyomar, 2008). At resonance, all circuits are capable of the same peak output but vary in the amount of piezoelectric material needed. Below resonance, the active circuits present an opportunity to greatly boost the specific output of the system since stiffness dominates the system. Using the SSHI circuit, for example, output can be increased up to 10 times when compared to DCIM (Lefevre et al., 2006). The DCIM circuit will be simulated to provide a baseline, and the SECE and SSHI circuits will be simulated to explore the maximum achievable output.

The authors have found no literature concerning power harvesting with piezo materials used close to their mechanical or electrical limits where voltage effects may cause depolarization or changes in capacitance of the piezo material. Yang et al. (2008) present a study on the variation of the capacitance of piezo material and found that the variation may be significant depending on the

voltage field and applied mechanical stress. The effect of these changes and what consequences they may have on the relative performance of various power harvesting circuits are explored. A generic nonlinear capacitance model is assumed for the second series of simulations.

The effects of fatigue are not considered in this study. This does not appear to be an issue as stresses and strains are kept below those presented as limitations by Gall et al. (2009). The electronics for control of the active circuits were also not considered. With respect to Guyomar et al. (2005) and Lefevre et al. (2005), it can be concluded that these control electronics will consume approximately 10% of the total available power. For the SSHI circuit, an example of the inversion circuitry is given by Lallart et al. (2007). The electronics required to condition the harvested power for further use are also not considered. Based on the aforementioned references, the total efficiency can be expected to be around 70%.

Modeling

The rotor of a helicopter consists of a number of components. Major structural components are the rotor hub, swashplate (for blade pitch control), and the blades. To allow for control of the craft, the motion of the swashplate is transmitted to the blades through pitch links that control the pitch of each blade. The blades are hinged on the rotor and are free to rotate in the vertical and horizontal directions, called the flapping and lead/lag motion, respectively.

During forward flight, a phenomenon called dissymmetry of lift arises. This results from the fact that blades moving forward relative to the rotorcraft see a higher relative airspeed compared to those moving backward. To ensure that the net lift is roughly above the center of gravity of the aircraft, the forward-moving blades have a lower pitch or angle of attack than the backward-moving blades. This creates a once-per-revolution variation in drag as well. The velocity distribution over the blade is shown schematically in Figure 1.

Where the variation in lift (distribution) per blade results in a flapping motion, the movement is sufficiently damped by the airflow due to the entire planform area of the blade moving through the air. The lead/lag motion, however, does not have so much

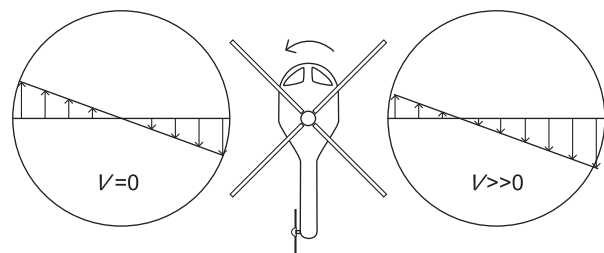


Figure 1. Velocity distribution for hovering (left) and forward flight (right). Curved arrow denotes blade rotation direction.

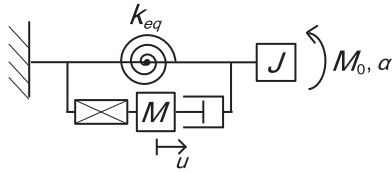


Figure 2. Mechanical IPM of the blade and modified damper. IPM: ideal physical model.

damping as it is the frontal area of the blade that must produce the required aerodynamic damping. Additionally, there are two dangerous phenomena called air and ground resonance, which relate primarily to the blades oscillating excessively in the rotor plane. To this end, a damper is installed over each blade hinge to provide additional damping in the lead/lag direction. The proposal is to augment this damper with a piezoelectric stack to generate electricity, which can be used for health monitoring equipment in the blade.

The ideal physical model (IPM) of the concept is shown in Figure 2. Only the rigid lagging motion is considered. It shows the stiffness k_{eq} , blade moment of inertia J , external applied moment M_0 , and the stack DOF u with associated mass M and α representing the blade angle. The mechanical model is modeled in *MATLAB* using *Simulink*'s plugin *Simscape*. Important lumped parameters k_{eq} and M_0 will be elaborated in the following paragraphs.

The damper under consideration is a nonlinear viscous damper. It is located 0.254 m from the blade hinge. The force generated increases rapidly to 9 kN at 25 mm/s after which a dump valve opens, limiting the force to 9 kN. This mode of operation becomes clear from the force–time curve as the force rises quickly and then reaches a plateau of 9 kN, see Figure 3(a) and (b)

showing the force and velocity for a flight speed of 130 knots. The variations associated with flexible lagging modes are not considered and will be shown to be negligible.

Dynamic data have been provided by *Agusta Westland (AW)*. As a simplification of the drag loads on the blade, a sinusoidal excitation with amplitude M_0 is applied. The amplitude is determined by equating the dissipated energy of the *AW* data to that of the model. It is found that $M_0 = 10.7$ kNm yields the same dissipation in the *Simulink* model.

Again considering Figure 3(a) and (b), *AW* data are represented by the dashed line. The lag damper mainly sees the rigid body mode of the blade in the lead/lag direction, which, as shown in Figure 3(a), is an acceptable assumption. The rigid blade assumption implied in Figure 2 is thereby justified. The spring constant k_{eq} of the IPM is calculated such as to achieve the same in-plane natural frequency of the blade resulting from centrifugal loads during flight. Further required blade data such as blade inertia are provided by *AW* (Maybury et al., 2009).

The resulting damper speed and force from the IPM are also shown in Figure 3(a) and (b) by the solid line. Close agreement is found for the peak damper loads with less than 1% difference between the *AW* data and the *Simulink* model. The presented simplified model is acceptable considering that the damper force is the main input for the stack.

Finally, no aerodynamic coupling is considered. Although a large stack is used, the additional damping this creates is small relative to the preexisting aerodynamic damping and when compared to the 250 W of the lag damper. Moreover, the harvesting frequency will be shown to be equivalent to the rotor rotation speed at which there is no direct excitation of resonance

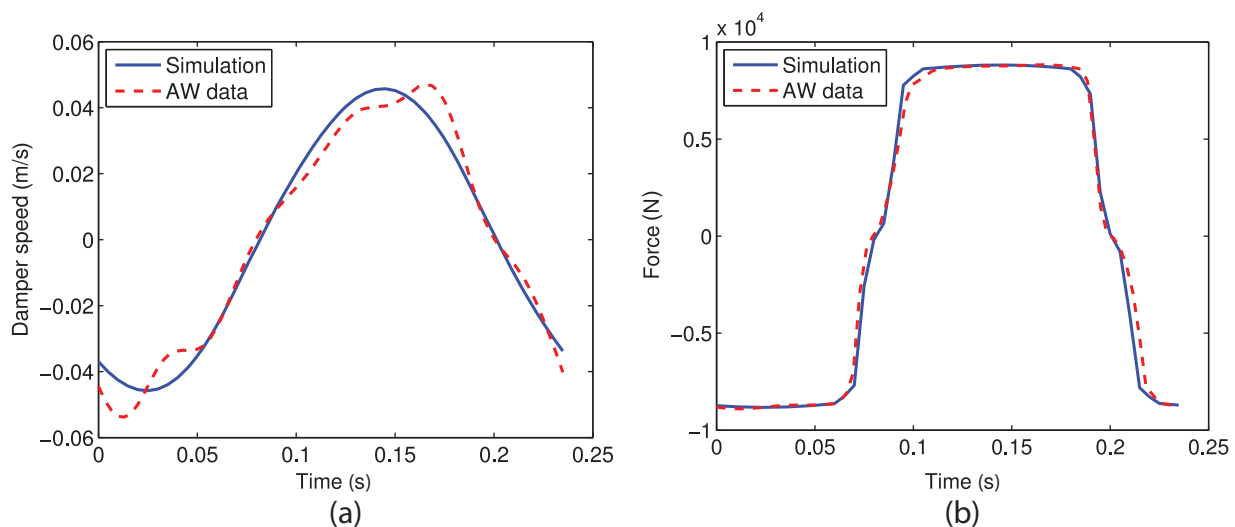


Figure 3. Comparison between *AW* data and *Simulink*: (a) damper velocity and (b) damper force. *AW*: Agusta Westland.

Table 1. Material data for PIC181 assuming plane stress.

Property	Value	Unit
Young's modulus (33 direction)	70	GPa
Piezoelectric coefficient, e_{33}	14.7	N/Vm
Relative permittivity, ϵ_{33}^{σ}	1135	—
Coercive field strength	2	MV/m
Maximum compressive stress, σ_{max}	120	MPa

modes. The first lag frequency (rigid motion) is 1.24 Hz, and the second is at 19 Hz (Maybury et al., 2009). The rotation frequency is at 4.18 Hz. Thus, the lag damper is excited mainly at a frequency where the blade can be considered as a rigid rotational inertia, and small additional damping will not influence the behavior.

Piezoelectric model

Hard lead zirconate titanate (PZT) from PI Ceramic is chosen (PIC181) for its mechanical strength and high coercive field strength of 2 MV/m. Depolarization at room temperature due to reverse voltage typically begins at approximately half this value (PI Ceramic, personal communication), denoted here as E_v . Table 1 gives the relevant material data of PIC181. Note that for the simulation, the capacitance equals 80% of the value resulting from the material data through the basic capacitance equation (2). This is due to the differences in material data measurement, stress effects in the stack, and inactive regions within the stack caused by the manufacturing process.

The piezoelectric stack is modeled as a current source (with current $\theta\dot{u}$) and capacitance (C_p) in parallel using the following fundamental equations (Priya and Inman, 2009)

$$k_p u(t) + \theta V_p(t) = F(t) \quad (1a)$$

$$\theta \dot{u}(t) - C_p \dot{V}_p(t) = I(t) \quad (1b)$$

and the following substitutions

$$k_p = \frac{EA}{nt_l} \quad \theta = \frac{e_{33}A}{t_l} \quad C_p = \frac{ne_{33}^{\sigma}A}{t_l} \quad (2)$$

with k_p , $u(t)$, θ , $V_p(t)$, $F(t)$, and $I(t)$ representing the piezo stack stiffness, displacement, piezoelectric coefficient, stack voltage, applied force, and electric current from the stack. The variables E , A , n , t_l , e_{33} , and e_{33}^{σ} represent Young's modulus, stack area, number of layers, layer thickness, piezoelectric coefficient, and permittivity in 33 direction at constant mechanical stress, respectively. A dot over a time-dependent variable denotes a derivative with respect to time. Note that the layers of the stack are electrically coupled in parallel.

The stack area is chosen as small as possible while remaining within the compressive stress limit of 120

MPa. The maximum stack length (L) available in the damper rod is 25 cm. Then a thickness of each layer must be chosen. There is no optimum layer thickness according to Roundy (2005) where it is concluded that only the volume of piezo material is relevant. In practice, however, layer thickness does influence the voltage and currents and in turn resistive losses as well. The influence of layer thickness, t_l , is therefore investigated. The electrode in between the layers is neglected as these can be less than 1% of the layer thickness.

Finally, a note on the electromechanical coupling k_e^2 , which is calculated as (Lefevre et al., 2005)

$$k_e^2 = \frac{\theta^2}{k_p C_p} \quad (3)$$

Due to the use of a stack, this reverts to the fundamental form using the material parameters

$$k_e^2 = \frac{e_{33}^2}{E \epsilon_{33}^{\sigma}} \quad (4)$$

In this system, the coupling is 0.38, meaning that the piezoelectric effect has a significant influence on the mechanical domain. The effect of coupling is most easily demonstrated by its effect on the fundamental natural frequency of a piezoelectric element (Shu and Lien, 2006a)

$$\omega_{oc} = \omega_{sc} \sqrt{1 + k_e^2} \quad (5)$$

where subscripts sc and oc denote short circuit and open circuit, respectively. Short circuit means no voltage is built up ($V(t) = 0$ for all t) and open circuit means all the developed charge goes toward generating the maximum possible voltage ($I(t) = 0$ for all t). For active circuits, this high coupling will show some effects.

Circuits and simulation results

The following section shows results using the *Simscape* model. *Simscape* allows multiple domains within one model and coupling between each domain. The electromechanical coupling is modeled using the current source representation analogous to equation (1b). Simulations are run using an implicit variable step solver using numerical differentiation formulas. The maximum timestep is chosen in the order of one-twentieth of the oscillation period of the highest natural frequency in the model. Adaptive zero-crossing is used to, for example, allow the solver to converge to the exact timestep when a diode goes into or out of conduction, allowing it to adjust the mass and stiffness matrices of the problem accordingly after the discontinuity.

All stated power figures are time-averaged values dissipated in the load resistor over the last cycle of the

simulation. This represents power delivered to an ideal load, and in reality, further conditioning electronics are necessary to control the output voltage for use in electronics. This will imply an extra loss over the final values presented here of around 10%. Finally, the components are considered linear or piecewise linear. The diodes have a single constant voltage drop, and transistors (for SSHI) have constant parameters, but in reality, these vary greatly as the limits of the component are approached. In reality, the components must be chosen with care.

DCIM simulations

The DCIM circuit consists of a full bridge rectifier, storage capacitor C_s , and resistive load R . The schematic is given in Figure 4, and Shu and Lien (2006b) give a detailed electrical and mathematical description of the circuit. Here, the peak stress limits geometry leading to a cross section of $A = 1.5 \text{ cm}^2$. The most important property is that for single frequency harmonic motion, an optimal resistance can be calculated as $R_{opt} = \pi / (2\omega C_p)$ with ω representing the excitation frequency of the harvester. Finally, the storage capacitance is determined from the standard capacitor-resistor differential equation such that the drop in voltage between charge cycles is no more than 3%.

The results are given in Figure 5. One line represents the power from the simulation as a function of the load resistance. The thickness of the piezoelectric layers shows minimal influence on the harvested power that peaks at 2.25 W. The optimal resistance does not agree with the basic equation for R_{opt} , which assumes low coupling but is in good agreement with the analytical solution by Shu and Lien (2006b) who maintain the presumption of significant coupling throughout their analysis. This yields an optimum resistance that is also a function of the electromechanical coupling factor.

The simple passive layout of this circuit negates the need for further investigation. The maximum performance found here is very close to the theoretical maximum (assuming lossless components) since only the diodes represent any significant loss in the form of a voltage drop over the component.

SECE

The SECE circuit shown in Figure 6 consists of a full bridge rectifier, a switched coupled inductor with inductances L_1 and L_2 diode, storage capacitor C_s , and resistor R . The research by Lefeuvre et al. (2005) provides a detailed description of the circuit operation. During use, the piezo element normally operates in an open circuit. As the displacement/voltage peaks, the switch S is briefly closed allowing the element to conduct through the coupled inductor and rectifier to the storage circuit.

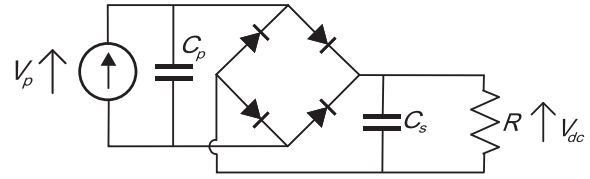


Figure 4. DC impedance matching circuit.
DC: direct current.

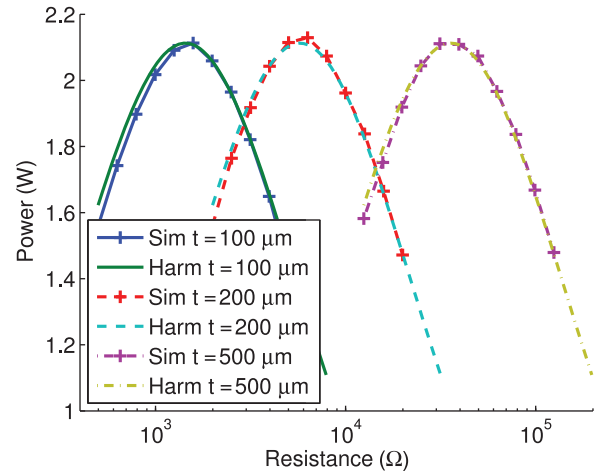


Figure 5. Power versus resistance for varying t_i . *Sim* denotes simulation results and *harm* denotes harmonic results from an analytical approach.

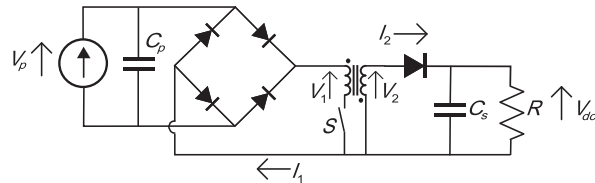


Figure 6. SECE circuit.
SECE: synchronous electric charge extraction.

The circuit achieves four times larger coupling than DCIM.

For the SECE circuit, the peak reverse voltage field (E_v) presents the limiting factor. From Lefeuvre et al. (2005) and assuming $\Omega \ll \omega$, the peak voltage can be calculated as

$$V_{p, \max} = 2 \frac{\theta}{C_p} u_0 = 2 \frac{\theta}{C_p} \frac{F_0}{k_p + \theta^2 / C_p} \quad (6)$$

where u_0 is calculated from equation (1b) for the open-circuit condition assuming $V_{p, \max} = E_v t_l$ (inherent to circuit operation) and applying a force F_0 . Solving for the stack area, this results in at least 3.32 cm^2 for the specified material and loading in order to prevent electrical overload. This area is significantly larger than what is

minimally required for the DCIM circuit, which is limited by the peak mechanical stress.

The inductance values, primary L_1 and secondary L_2 , are calculated based on the desired discharge duration. In these simulations, the natural frequency of the capacitor–inductor loop is arbitrarily chosen as 100 Ω . The required inductance as a function of the natural frequency and stack capacitance time follows from the natural frequency of an electrical oscillator

$$L_1 = \frac{1}{\omega_{el}^2 C_p} \quad (7)$$

where variables ω_{el} and L_1 represent the electrical natural frequency and primary inductance of the coupled inductor. The inductor quality factor $Q_i = \omega_{el} L_1 / R_{coil}$ is a measure of how much damping is present in the system with a higher Q_i indicating fewer losses.

The discharge time of the inductor in the secondary circuit is determined as such to prevent undesired overlap of the primary and secondary currents. This is caused by the significant electromechanical coupling ($k_e^2 = 0.38$) of the stack. After discharging, the stack settles to a new equilibrium but charges while doing so due to the piezoelectric effect.

The current in the secondary circuit should be zero before such a secondary discharge event occurs. A constant DC voltage V_2 and quasi-static state are assumed. Ignoring the effects of the diode, the secondary inductance L_2 is calculated as follows

$$\frac{1}{2} C_p V_1^2 = \frac{1}{2} L_2 I_2^2 \quad \rightarrow \quad \Delta I_2 = \sqrt{\frac{C_p}{L_2}} V_1 \quad (8a)$$

$$P = \frac{1}{2} C_p V_1^2 \frac{\Omega}{\pi} = \frac{V_2^2}{R} \quad \rightarrow \quad V_2 = \sqrt{\frac{1}{2} C_p \frac{\Omega}{\pi} R V_1} \quad (8b)$$

$$V_2 = L_2 \frac{dI_2}{dt} \quad \rightarrow \quad L_2 = \frac{\Omega R t_{off}^2}{2\pi} \quad (8c)$$

Time t_{off} is the time taken to discharge the secondary coil from I_2 , shown schematically in Figure 7. The gradient of the graph is constant because the storage capacitance C_s is chosen sufficiently large implying a constant voltage V_2 . From this, I_2 is calculated as in equation (8a), which equates the incoming and outgoing energies of the coupled inductor for a single charge/discharge event. Voltage V_2 is determined from the energy content of the fully charged piezo stack multiplied by twice the excitation frequency (Ω/π) (equation 8(b); Lefeuvre et al., 2005). These equations are combined in the fundamental equation for a linear inductor yielding the secondary inductance as a function of frequency, desired discharge time and load resistance. It can be derived that inclusion of the conversion efficiency of the coupled inductor does not influence the secondary inductance value.

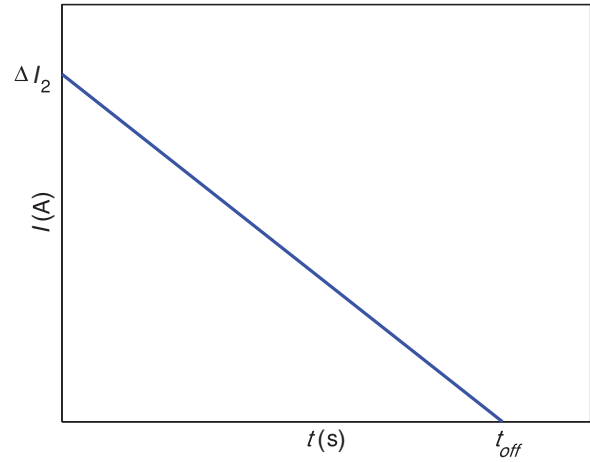


Figure 7. Schematic of the secondary inductor current discharge.

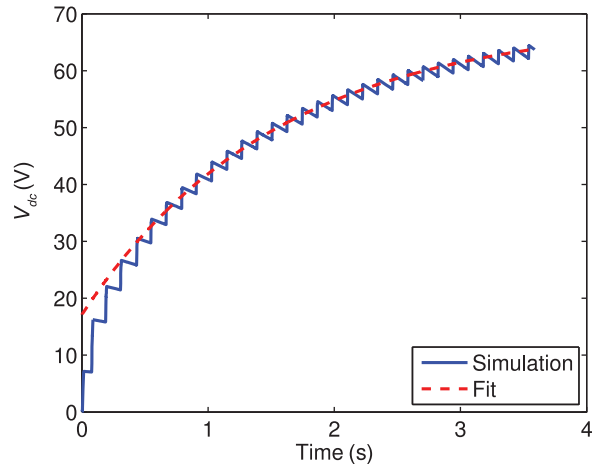


Figure 8. Voltage simulation and curve fit example.

The power is calculated by simulating the system for a number of cycles. A curve fit is then performed on part of the time history as shown in Figure 8. The solution of the differential equation of a charging capacitor in parallel with a resistor and current source is used

$$V = C_1 e^{\frac{C_2 - t}{C_3}} + C_4 \quad (9)$$

where C_n represent the unknowns. The limit voltage is given by $C_1 + C_4$ and is used to calculate the power, $P = V^2/R$. The last 1.5 s of the simulation are used for the fitting process, avoiding transient effects from the mechanical domain. This simulation is performed for varying load resistance and layer thickness. Aside from the conclusions by Lefeuvre et al. (2005), it is also found that power output is reduced for small thicknesses (up to 200 μm). This is due to the higher capacitance and associated currents ($I_{1,max} \approx 9 \text{ A}$ for $t_l = 100 \mu\text{m}$) and resistive losses in the circuitry.

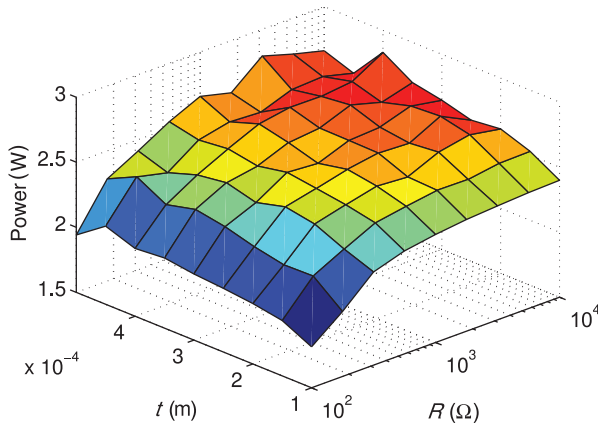


Figure 9. Power versus layer thickness and load.

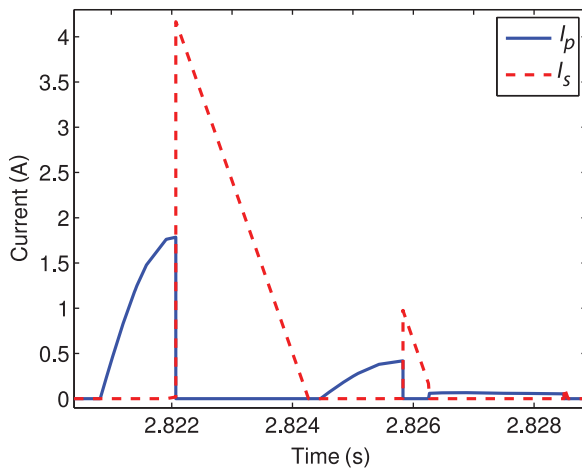


Figure 10. Primary and secondary inductor currents.

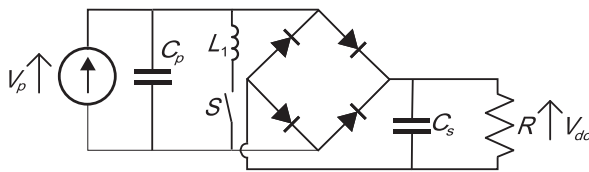


Figure 11. SSHI circuit.

SSHI: Synchronized Switch Harvesting on Inductor.

The power dissipated in the resistor is approximately 2.6 W, although the roughness of Figure 9 implies some inaccuracy. The power determined from the discharging of the piezo stack is 2.9 W, yielding an efficiency of 89%. This is quite high although the additional power from the secondary discharges, shown in Figure 10, account for 5% of the output. These are not foreseen by Lefeuvre et al. (2005). Also, the control electronics are not considered in this simulation, reducing the efficiency. The switching electronics must be powered from the stack itself and depending on the chosen topology will reduce the efficiency in the order of 10%.

Hence, from the discussion of the SECE circuit, the results show that 2.6 W of power can be generated. A number of aspects in the design of the SECE circuit for highly coupled electromechanical systems have been identified. The reverse bias represents the most crucial limitation resulting in a large stack cross section and greatly decreasing the effectiveness of the circuit. The high coupling implies that some care must be taken in determining the load, inductance, and capacitance of the DC part of the circuit.

SSHI

This circuit (Figure 11) resembles the DCIM circuit with the addition of a switched inductor between the contacts of the piezo element, creating a capacitor–inductor oscillator. The switched inductor is used to invert the piezo voltage at displacement extrema. This circuit also possesses an optimal resistance, but it is typically much higher than that of the impedance matching circuit. Guyomar et al. (2005) and Shu et al. (2007) provide a more detailed electrical and mathematical description. First, the power equation will be derived and the important variables will be addressed. Second, a number of operational aspects related to optimizing the output will be discussed.

As with the SECE circuit, the voltage is the limiting factor in the system. Considering the high stress that is applied, it will be shown that it is not possible to use the optimal resistance associated with the circuit. The resulting piezo voltage would then exceed the maximum reverse bias of the material. An optimum must be found between the stack area A , load resistance R , and maximum voltage field E_v . The maximum resistance allowed for a given E_v can be calculated from equation (7) in Shu et al. (2007). Since the lag damper is operated far below the resonance of the piezo stack, a first-order approximation for the excitation frequency ω is justified. The equation is then rewritten to give R as a function of the maximum voltage and stack geometry, yielding

$$R = \frac{-V_{p,max} \pi k_p}{\Omega \left(2F_0 \theta - V_{p,max} \left(1 - e^{\frac{\pi}{2\theta}} \right) (\theta^2 + k_p C_p) \right)} \quad (10)$$

Using the resistance found through the above equation and the maximum reverse bias of the material, the resulting power can be calculated from $P = V^2/R$. Rewriting the variables of geometry and material data yields

$$P = \frac{1}{E} E_v A L \Omega \left(2 \frac{F_0}{A} e_{33} - E_v \left(1 - e^{\frac{\pi}{2\theta}} \right) (e_{33}^2 + E \varepsilon_{33}^\sigma) \right) \quad (11)$$

Equation (11) can then be used to determine the optimum stack geometry. The choice of material

determines the piezoelectric voltage constant e_{33} , maximum reverse bias, and permittivity. Three other input values remain: stack length L , cross section A , and the inversion quality factor Q_i . Deriving the power equation to each shows that increasing stack length, reducing the cross section, and maximizing Q_i consistently increase power output. These are limited to $L = 0.25$ m due to available space, $A = 1.5$ cm² due to mechanical stress, and order 10^2 resulting in 7.8 W of power. In equation (11), the first term in the brackets represents the charge generated by the piezoelectric effect and the second negative term the losses due to voltage inversion.

Inversion duration. Note that Shu et al. (2007) do not use the inversion duration in their calculations. For resonant or low-coupled systems, this is no issue but a highly coupled subresonant system will oscillate at its mechanical natural frequency ω_{mech} following voltage inversion. The inversion frequency ω_{inv} determines how much the mechanical domain will be excited with a lower ω_{inv} leading to a lower excitation. Due to the strong electromechanical coupling, ω_{inv} is not identical to the natural frequency of the electrical circuit alone ($\omega_{elec} = 1/\sqrt{L_1 C_p}$) but is found by solving the complex eigenvalue problem of the coupled stack including both mechanical and electrical domains. Here, it is presumed that the DOF of the blade has minimal influence and that the rectifier is blocked, reducing the electrical circuit to a linear system. Compared with equation (1b), current $I(t)$ is zero, and the inductive term is added. Parameter R_L is the resistance of the coil which is determined by the quality factor.

$$\begin{bmatrix} M & 0 \\ 0 & C_p \end{bmatrix} \ddot{q} + \begin{bmatrix} C & \theta \\ -\theta & R_L \end{bmatrix} \dot{q} + \begin{bmatrix} k_p & 0 \\ 0 & \frac{1}{L_1} \end{bmatrix} q = 0, \quad (12)$$

$$\dot{q} = \begin{pmatrix} \dot{u} \\ V \end{pmatrix}$$

A calculation of the full 3-DOF system (circuit voltage, stack, and blade position) reveals a difference of 0.1% in the electromechanical natural frequency, justifying the omission of the blade DOF. As demonstrated in Figure 12, voltage inversion duration influences viscous losses in the mechanical domain. The horizontal axis shows the time normalized with the respective inversion time $t\omega_{inv}/(2\pi)$ and the vertical axis the normalized voltage $V/V_{p,max}$. Note that $Q_i = 100$ for both cases. Perfect inversion would mean the normalized voltage settles at -1 .

For slow inversion (dashed line), the voltage inversion is stopped at the optimum point and then remains stable. The fast inversion case (solid line) initially achieves better inversion at $t\omega_{inv}/(2\pi) = 1$. However, the mechanical domain begins to oscillate. Only the

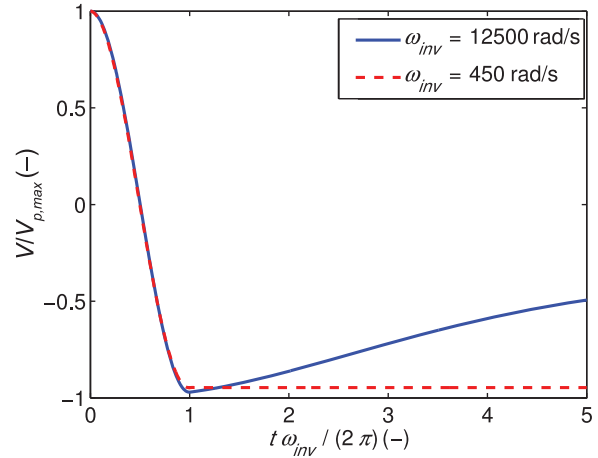


Figure 12. Stack voltage against dimensionless time during inversion.

onset of the oscillation is shown in Figure 12 where the amplitude slowly increases from -0.98 to oscillate around -0.45 . Due to the high damping of the lag damper, this energy is dissipated within one oscillation. Ideally the inversion should take as long as possible to minimize losses. Considering the damper force–time graph of Figure 3(b), the maximum inversion time is limited to 0.02 s. However, in combination with the large stack, the required inductance may become unrealistically large to install in the rotor of a helicopter, representing a constraint on the system.

Up to 95% inversion can be achieved for a high Q_i and long inversion duration. In reality, this number will be reduced due to less than ideal components. The mechanical and electrical natural frequencies should be chosen as high and as low as possible, respectively. The mass of the piston is shown to be an important variable in this design.

As a brief qualitative note, assuming linear behavior and perfect voltage inversion, the power dissipated by the viscous damper due to inversion can be written as Meirovitch (2001)

$$P = c\omega_{inv}u_0^2\Omega \rightarrow P = c\omega_{inv}\left(\frac{2e_{33}LE_v}{E}\right)^2\Omega \quad (13)$$

with c and u_0 a constant damping coefficient and the displacement amplitude during inversion, respectively. Qualitatively, the power dissipated decreases quadratically with stack length. As the inductance, through ω_{inv} , roughly has a $1/\sqrt{L_1}$ relationship in this equation, the inductance values quickly becomes small enough that it becomes a nonissue for shorter stacks. For example, the stack length is reduced by 5 cm from the previous simulations to a total of $L = 20$ cm. This requires an inductance of only 10 mH for $t_l = 60$ μ m versus the 50 mH limit used in all other SSHI simulations to achieve the same volume-weighted specific output.

Table 2. Input data SSHI model.

Variable	Symbol	Unit	Value
Stack area	A	m^2	1.5×10^{-4}
Stack length	L	m	0.25
Maximum voltage field	E_v	V/m	10^6
Layer thickness	t_l	m	$(10 \dots 200) \times 10^{-6}$
Elasticity modulus PIC181	E	N/m^2	71×10^9
Piezoelectric coefficient	e_{33}	N/Vm	14.7
Relative permittivity	$\epsilon_{33,r}^\sigma$	—	0.8×1135
Inductor quality	Q_i	—	100
Stack viscous damping	ζ	—	10^{-2}
Piston (DOF) mass	m_{piston}	kg	1
Rotor angular velocity	Ω	rad/s	26.26
Blade moment of inertia	J	kgm^2	2387
Equivalent hinge stiffness	k_{eq}	Nm/rad	1.43×10^5
Damper moment arm	r	m	0.254
Excitation moment amplitude	M_0	Nm	1.07×10^4
Simulation time (80 blade oscillations)	t_{max}	s	19.14
Storage capacitor discharge ratio	DT	—	0.97

SSHI: Synchronized Switch Harvesting on Inductor; DOF: degree of freedom.

General results. Table 2 summarizes all input data governing the constant capacitance SSHI simulation model. The stack viscous damping number is taken from Zheng et al. (1993) but has no influence on the results due to the high damping of the lag damper. The storage capacitor discharge ratio is the same as discussed for the DCIM circuit in section “Circuits and simulation results.”

Figure 13 shows the results for the SSHI circuit. The power is plotted against the inversion time for various layer thicknesses. The influence of the inversion time is again emphasized by the fact that submillisecond inversion times yield only 5 W of power compared to more than 7 W for inversion times in the order of 10 ms. Layer thickness shows minimal influence on output and is clearly not of importance with regard to output.

Figure 14 shows a close-up view of the high-output area. Lines corresponding with larger thicknesses terminate at shorter inversion times. This is to demonstrate the effect of the inductor value as a practical limitation. Although 50 mH is chosen arbitrarily as a limit value, such inductors and the required current capacity of 3 A start to become large and heavy and may eventually become prohibitive for use in helicopters. As layer thickness determines the capacitance, and therefore the required inductance, it does represent an important variable.

This figure also indicates a limit to the inversion time above which only marginally more power may be harvested. The peak power value found in Figure 13 (7.0 W at $R = 317 \Omega$, $t_{inv} = 6$ ms, $t_l = 50 \mu m$, $V_{p,max} = 49.5$ V) corresponds well with the value found when using the analytical model presented by Shu et al. (2007), which yields 7.15 W at 338Ω and $V_{p,max} = 500$ V.

Figures 15 and 16 show detailed results based on a layer thickness of $60 \mu m$, $t_{inv} = 6$ ms and $Q_i = 100$. These input variables allow for maximum power, the lowest inductor currents and without exceeding the inductance limit. It represents one data point in Figure 13. For this geometry, peak switching current is nearly 3 A and 7.3 W of power is generated at 59 V.

The inductor efficiency Q_i here is chosen as 100 which is quite a high value. Table 3 shows some results for varying inductor quality at ω_{inv} . For clarity, the inversion efficiency V_2/V_1 is also given. The switching circuitry may influence this efficiency, so some investigation into the influence of this variable is justified. Lefeuvre et al. (2006) show that the output is very sensitive to this variable but do not consider the fact that the maximum reverse bias of the material may be exceeded, which is the case in these simulations. The values in Table 3 are given with the load resistor retuned to ensure maximum power. These data cover the entire range for Q_i from very poor to exceptional quality and gives lower and upper bounds for the power output from the circuit.

Comparing the data to the results from Lefeuvre et al. (2006) the condition of a maximum reverse voltage makes the circuit much less dependent on the inversion quality. Although there is still a clear influence, there are no order of magnitude changes in the output for a modest increase in the induction quality.

Finally, the dynamics of the mechanical domain must be considered to ensure the safety of the rotorcraft. Figure 16 gives the normalized force, and this shows strong resemblance to the original force diagram of the lag damper alone in Figure 3(b). The main difference is a momentary drop in force just when it peaks. This drop is a result of the high electromechanical

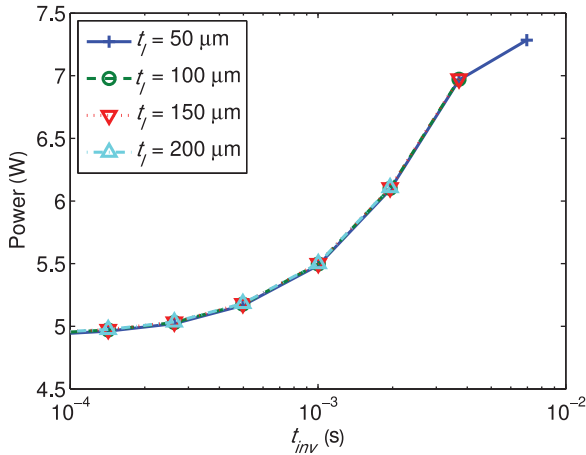


Figure 13. SSHI output, general impression. SSHI: Synchronized Switch Harvesting on Inductor.

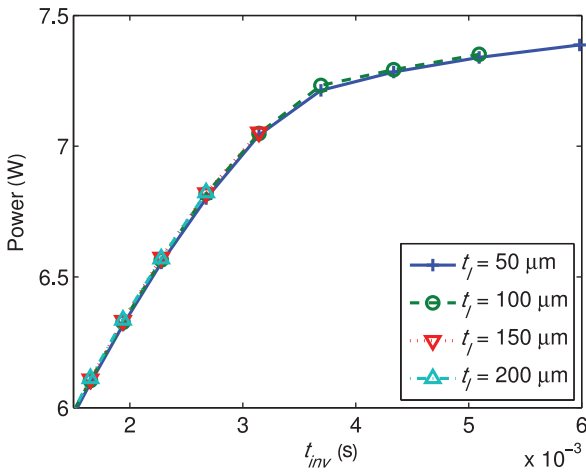


Figure 14. SSHI output, area of interest. SSHI: Synchronized Switch Harvesting on Inductor.

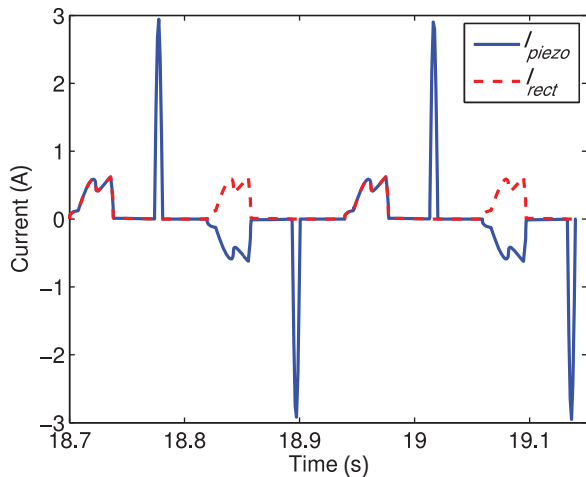


Figure 15. SSHI current for $t_l = 60 \mu\text{m}$ and $t_{inv} = 6 \text{ms}$. SSHI: Synchronized Switch Harvesting on Inductor.

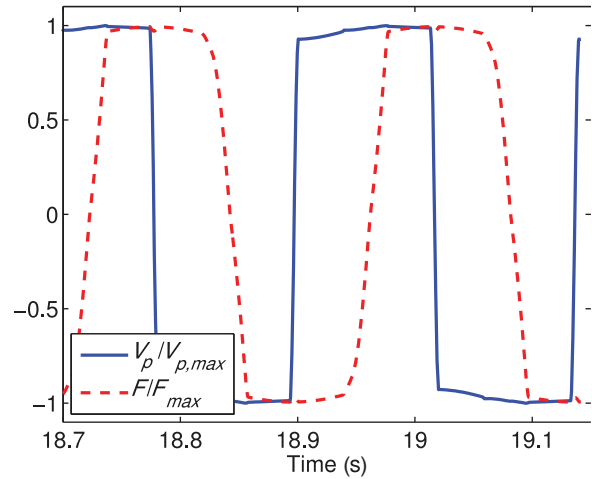


Figure 16. Normalized force on and voltage over piezo stack.

Table 3. Power output for varying Q_i .

Q_i (—)	Inversion efficiency (—)	Power (W)
100	0.98	7.3
20	0.92	7.0
10	0.85	6.7
5	0.73	6.2
3	0.59	5.7

coupling and voltage inversion of the stack. Figure 17 shows such an occurrence. The severity of the drop in force is determined by the inversion duration. Quick inversion will lead to a force variation in the order of kilonewtons (or 25% of the peak force), and slow inversion leads to only a few percent change. In the interest of helicopter safety, stability, and comfort, this force variation must be limited.

Nonlinear capacitance model and temperature effects

According to Yang et al. (2008), there is a strong nonlinearity in the capacitance of piezo material. They show that particularly low mechanical stresses and high voltage fields can lead to a more than 10-fold increase in capacitance. This will have a profound effect on all previous derivations and simulations. New simulations are conducted without any analytical evaluation. This is due to the impossibility of deriving a new optimal operating point for any of the circuits considered. It is also impractical in real systems that will require intelligent control or nonlinear passive circuits to control discharge and inversion as operating conditions change. The nonlinear capacitance that is used is only considered to be dependent on the prevalent voltage field and is shown in Figure 18. More complex models that are

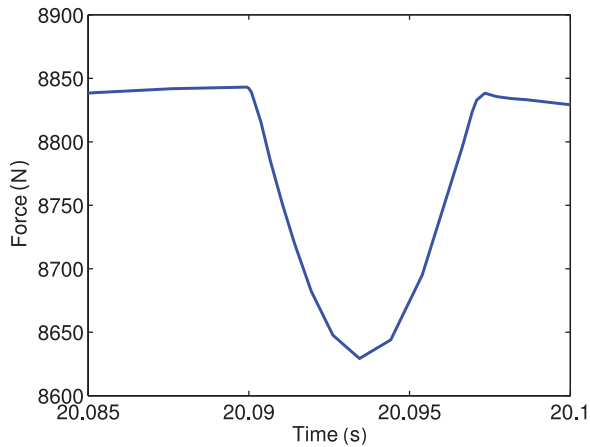


Figure 17. Force variation around one voltage inversion event for $t_{inv} = 6$ ms.

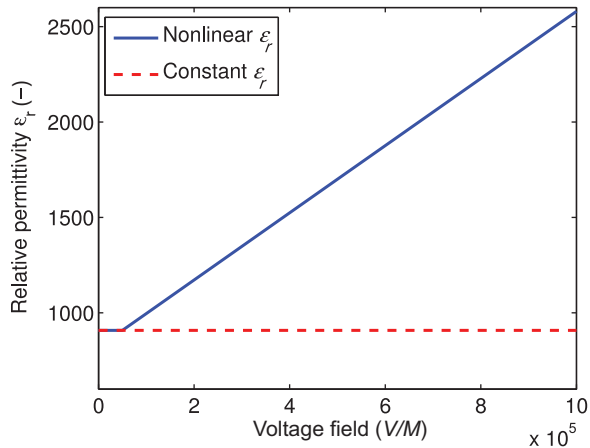


Figure 18. Nonlinear capacitance model.

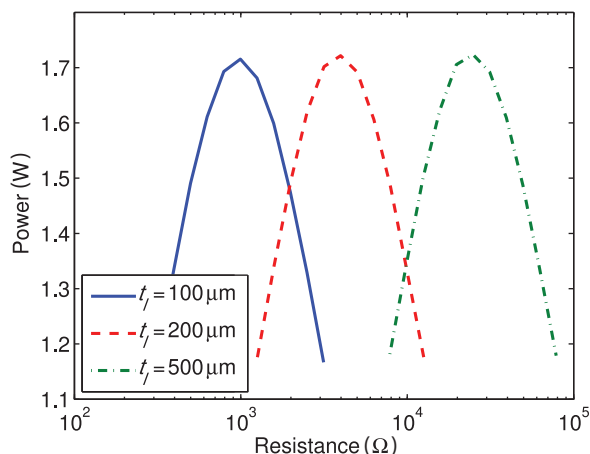


Figure 19. DCIM, nonlinear C_p power output. DCIM: direct current impedance matching.

based on real measured components may be used in the future for experimental validation. Unless noted the

Table 4. SECE performance for linear and nonlinear capacitance models, $t_i = 500$ μ m.

	Stack area (cm^2)	$V_{p,max}$	Power (W)
Linear capacitance model	3.32	500	2.6
Nonlinear capacitance model	3.32	346	2.4
Modified nonlinear capacitance model	2.0	500	3.6

SECE: synchronous electric charge extraction.

simulations are run with the same parameters as the linear models discussed earlier as given in Table 2.

For the DCIM circuit, a new optimum resistance will need to be found. The results are shown in Figure 19. The higher capacitance not only leads to lower optimum resistances but the output is also decreased by 25%. With the same amount of charge displaced by the piezoelectric effect, the higher capacitance yields lower voltages.

For the SECE circuit, it is possible to alter the stack area. In the constant capacitance case, the stack area is the main cause of the poor performance. The maximum reverse bias may be exceeded if the area is too small, so the mechanical stress applied was much less than the specified maximum: 50 MPa versus 120 MPa. With the increasing capacitance of the nonlinear case, more charge is required to charge the stack to a given voltage, allowing for a smaller cross section. The smaller stack area allows more charge generation from a given force. For the specified voltage–capacitance curve, the stack area can be reduced to 2.0 cm^2 , as opposed to 3.32 cm^2 for the constant capacitance case, before the maximum reverse bias is exceeded. The resulting power is 3.6 W, an increase of over 38%. Here, the increasing capacitance is clearly to the advantage of the SECE circuit. Table 4 provides clarification.

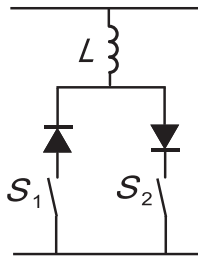
The SSHI circuit shows only a minimal loss in output. The consequences of the increasing capacitance are twofold: first, it requires more cycles to charge the stack to a specified voltage since more charge must be accumulated for a given voltage. Second, more charge leads to higher losses during voltage inversion and a lower operating voltage when otherwise the same settings are used for the constant capacitance case. The output is then reduced, but an advantage of the SSHI circuit here is that the load resistance can be retuned to compensate for some of the losses. Table 5 summarizes the linear and nonlinear capacitance cases.

Another consequence of the nonlinear capacitance is that the inversion time becomes voltage dependent. Now the switch triggering the inversion must be closed sufficiently long to accommodate full inversion with a diode added to prevent reverse current once inversion is complete. A second switch S_2 and diode combination must be added to allow for inversion in the opposite

Table 5. SSHI performance for linear and nonlinear capacitance models, $t_f = 60 \mu\text{m}$.

	Resistance (Ω)	$V_{p, \max}$	Power (W)
Linear capacitance model	471	59.7	7.3
Nonlinear capacitance model	471	57.5	6.7
Retuned nonlinear capacitance model	495	60	7.0

SSHI: Synchronized Switch Harvesting on Inductor.

**Figure 20.** Expanded switching circuitry for nonlinear SSHI circuit.

SSHI: Synchronized Switch Harvesting on Inductor.

direction. The switch in the circuit of Figure 11 is then replaced by the switching circuitry given in Figure 20. A design of such a (self-powered) switch is given by Lallart et al. (2007).

Ambient temperature has a notable effect on piezo performance. In the simulations presented in this article, the material is highly stressed, and the maximum reverse bias is a critical factor. This value decreases to zero when the Curie temperature is reached. For 70°C , the reverse bias is decreased by approximately 30% from room temperature (PI Ceramic, personal communication). Table 6 summarizes the effects of the increased temperature on the nonlinear capacitance harvesting models using $E_{V, \max} = 0.7 \text{ MV/m}$, a 30% reduction from the value at room temperature.

The DCIM circuit suffers no additional loss due to the voltage field reaching only 0.17 MV/m . The reduced reverse bias limit is no issue since in this circuit, the material is stress limited. For the SECE circuit, the

voltage field can only be limited by increasing the stack area as the material is stressed in open-circuit mode most of the time. This leads to a large cross section, reducing the applied stress and resultant piezoelectric performance. When the SECE circuit is used, the stack must be designed for the worst case scenario, greatly reducing the output during normal operation. The SSHI circuit can again be adjusted by means of the load resistance. Similar to the varying capacitance case, this reduces the system voltage to an acceptable level. When the SSHI circuit is desired, a slender stack can be used, dimensioned to cope with the mechanical loads and maximizing the piezoelectric effect by tuning the load resistance.

Conclusion

Three circuits have been simulated in conjunction with a power harvesting lag damper: DCIM, SECE, and the synchronous switch harvesting on inductor circuit. Constant parameter models have been investigated, but nonlinear piezo material capacitance is an important factor, which has subsequently been included using a basic model.

It has been shown that the capacitance has a profound and varying effect depending on the circuit. Voltage-limited harvester designs benefit from the increasing capacitance as it allows a smaller stack and more efficient use of the piezo material. Mechanical stress-limited designs incur a loss as the piezo material generates less voltage for a given charge displacement.

The SSHI circuit is the best performing circuit, which has been evaluated for the lag damper. Assuming 130-knot forward flight, it provides up to 5.1 W of power from the largest possible stack ($1.5 \text{ cm}^2 \times 25 \text{ cm}$). This value takes nonlinear capacitance and elevated operating temperatures into consideration. The SSHI circuit can also be tuned through electrical means allowing for a stack with minimal cross section that yields the best performance. For the DCIM and SECE circuit in particular, the stack must be designed for the least favorable scenario to prevent electrical overload that greatly reduces output under more typical operating conditions.

Table 6. Changes in optimal geometry and performance for increased operating temperature.

Temperature ($^\circ\text{C}$)	Circuit	Area (cm^2)	t_f (μm)	R (Ω)	P (W)
20	DCIM	1.5	200	1000	1.7
	SECE	2.0	500	1783	3.6
	SSHI	1.5	60	495	7.0
70	DCIM	1.5	200	1000	1.7
	SECE	3.3	500	1783	2.3
	SSHI	1.5	60	346	5.1

DCIM: direct current impedance matching; SECE: synchronous electric charge extraction; SSHI: Synchronized Switch Harvesting on Inductor.

One word of caution concerns the components. They must be chosen to handle the high currents present in some cases with minimal losses. Most important are the transistors and diodes in the SSHI self-powered switching circuit (Lallart et al., 2007), which must pass the main switching current.

This amount of power is more than sufficient to power efficient strain gauges, which consume in the order of microwatts (Olson et al., 2008), wireless transmitters requiring 10–100 mW (Arms et al., 2005) and is nearing the consumption of fiber-optic systems in the order of 20 W. The consumption of fiber-optic systems is expected to decrease over the next few years. Therefore, a production model of the harvester will likely not be as large as what has been considered in this report, but the length can be tailored to the power requirements of the health monitoring systems.

Established optimization guidelines presented in literature are not applicable when expanding the operating envelope of piezo materials. The characteristics of some circuits lead to decreased performance as material limitations play a more critical role in, for instance, the SECE circuit than the SSHI.

No flight simulations have been conducted including the effects of the harvester system, but it is anticipated that the effect on flight dynamics will be minimal. When properly designed, the SSHI circuit will cause only minor changes in the damper loads in the order of a few percent. This system is a viable concept in extending the life of helicopter rotor blades.

Funding

This study is funded by the Clean Sky Joint Technology Initiative (grant number (CSJU-GAM-GRC-2008-001)9)—GRC1 Innovative Rotor Blades, which is part of the European Union's 7th Framework Program (FP7/2007-2013).

Acknowledgements

The authors are grateful toward Agusta Westland helicopters for providing relevant flight and dynamics data.

References

- Arms SW, Townsend CP, Churchill DL, et al. (2005) Power management for energy harvesting wireless sensors. In: *SPIE international symposium on smart structures and smart materials*, San Diego, USA, 9 March.
- Dietl JM and Garcia E (2010) Beam shape optimization for power harvesting. *Journal of Intelligent Material Systems and Structures* 21: 633–646.
- Feenstra J, Granstrom J and Sodano H (2008) Energy harvesting through a backpack employing a mechanically amplified piezoelectric stack. *Mechanical Systems and Signal Processing* 22: 721–734.
- Gall M, Thielicke B and Schmidt I (2009) Integrity of piezoceramic patch transducers under cyclic loading at different temperatures. *Smart Materials and Structures* 18: 1–10.
- Guyomar D, Badel A, Lefeuvre E, et al. (2005) Toward energy harvesting using active materials and conversion improvement by nonlinear processing. *IEEE Transactions on Ultrasonics, Ferroelectrics and Frequency Control* 52: 584–595.
- Harris NR, Beeby SP, Tudor MJ, et al. (2010) Thick-film piezoelectric vibration harvesting—a hums application. In: *APCOT*, 6–9 July, The University of Western Australia.
- Jeon YB, Sood R, Jeong JH, et al. (2005) MEMS power generator with transverse mode thin film PZT. *Sensors and Actuators A: Physical*.
- Lallart M and Guyomar D (2008) An optimized self-powered switching circuit for non-linear energy harvesting with low voltage. *Smart Materials and Structures* 17: 1–8.
- Lallart M, Lefeuvre E, Richard C, et al. (2007) Self-powered circuit for broadband, multimodal piezoelectric vibration control. *Sensors and Actuators A: Physical* 143: 377–382.
- Lefeuvre E, Badel A, Richard C, et al. (2005) Piezoelectric energy harvesting device optimization by synchronous charge extraction. *Journal of Intelligent Material Systems and Structures* 16: 865–876.
- Lefeuvre E, Badel A, Richard C, et al. (2006) A comparison between several vibration-powered piezoelectric generators for standalone systems. *Sensors and Actuators A: Physical* 126: 405–416.
- Maybury W, D'Andrea A, Hilditch R, et al. (2009) *Baseline blade definition for grc1.1*. GRC Report CS JU/ITD GRC/RP/1.1/31002, Green Rotorcraft.
- Meirovitch L (2001) *Fundamentals of Vibrations*. McGraw Hill. McGraw Hill, NY: Springer.
- Olson SP, Castracane J and Spoor RE (2008) Piezoresistive strain gauges for use in wireless component monitoring systems. In: *IEEE*, New York, 12–14 February, SAS. IEEE.
- Priya S and Inman D (2009) *Energy Harvesting Technologies*. Springer.
- Roundy S (2005) On the effectiveness of vibration based energy harvesting. *Journal of Intelligent Material Systems and Structures* 16: 809–823.
- Shu YC and Lien IC (2006a) Analysis of power output for piezoelectric energy harvesting systems. *Smart Materials and Structures* 15: 1499–1512.
- Shu YC and Lien IC (2006b) Efficiency of energy conversion for a piezoelectric power harvesting system. *Journal of Micromechanics and Microengineering* 16: 2429–2438.
- Shu YC, Lien IC and Wu WJ (2007) An improved analysis of the SSHI interface in piezoelectric energy harvesting. *Smart Materials and Structures* 16: 2253–2264.
- Yang G, Yue Z, Ji Y, et al. (2008) Dielectric nonlinearity of stack piezoelectric actuator under the combined uniaxial mechanical and electric loads. *Journal of Applied Physics* 104: 074116-1–074116-6.
- Zheng B, Chang C-J and Gea HC (2009) Topology optimization of energy harvesting devices using piezoelectric materials. *Structural and Multidisciplinary Optimization* 38: 17–23.
- Zheng J, Perez RJ and Lavernia EJ (1993) Documentation of damping capacity of metallic, ceramic and metal-matrix composite materials. *Journal of Materials Science* 28: 2395–2404.